



1 **Enigmatic Fe-Mn-fueled Anaerobic Oxidation of Methane in sulfidic coastal**
2 **sediments of the Eastern Arabian Sea**

3 **Kalyani Sivan^{1,2}, Aditya Peketi^{1,2}, Aninda Mazumdar^{1,2}, Anjali Zatale^{1,2}, Sai Pavan**
4 **Kumar Pillutla^{2,3}, Ankita Ghosh^{1,2}, Mohd Sadique^{2,3}, Jittu Mathai²**

5 ¹*Academy of Scientific and Innovative Research (AcSIR), Ghaziabad-201002, India*

6 ²*Gas hydrate Research Group, CSIR-National Institute of Oceanography, Dona Paula,*
7 *Goa-403004, India*

8 ³*School of Earth, Ocean, and Atmospheric Sciences, Goa University, Taleigao Plateau,*
9 *Goa-403206, India*

10 *Correspondence to:* Dr. Aninda Mazumdar, email: (maninda@nio.org)

11 **Abstract**

12 Anaerobic oxidation of methane (AOM) coupled with Fe-Mn reduction (Fe-Mn-AOM) is
13 considered a globally important biogeochemical process in marine sediments in addition to
14 sulfate-driven AOM (SO₄²⁻-AOM) responsible for the consumption of methane, a strong
15 greenhouse gas. Most existing studies have emphasized the significance of Fe-Mn-AOM
16 activities in sediments below the depth of the sulfate methane transition zone (SMTZ) with
17 insignificant dissolved sulfide and sulfate concentrations in the porewaters. Here, we report for
18 the first time enigmatic geochemical evidence of focused Fe-Mn-AOM activity across the
19 SMTZ in the presence of high dissolved sulfide concentrations in a sediment core collected
20 within the seasonal coastal hypoxic zone of the Eastern Arabian Sea (West coast of India
21 (WCI)). The Fe-Mn-AOM activity is evident from the concurrent decrease in CH₄
22 concentrations, δ¹³C_{CH4} and δ¹³C_{DIC} values coupled with the enrichment of porewater Fe²⁺ and



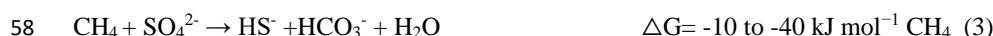
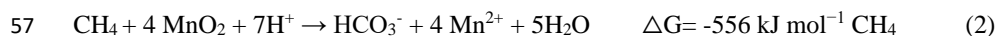
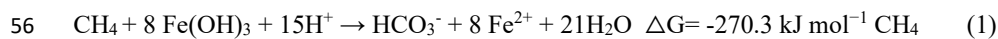
23 Mn^{2+} concentrations at multiple depths below the seafloor. Since neither CH_4 nor reactive Fe
24 appears to be the limiting factor controlling the Fe-Mn-AOM activity, we hypothesize that the
25 focused Fe-Mn-AOM at multiple depths is likely fueled by the localization of metal-reducing
26 and methanotrophic microbial communities, leading to biogeochemical heterogeneity in a
27 dynamic seasonally hypoxic coastal environment sensitive to climate change. This study
28 highlights new insight into CH_4 -S-Fe-Mn biogeochemical cycling with far-reaching
29 implications in climate studies linked to the estimation of sedimentary methane production and
30 consumption.

31 **1 Introduction**

32 The metal-driven anaerobic oxidation of methane (AOM) is a vital biogeochemical process
33 and may have a significant impact on global biogeochemical cycles, particularly in relation to
34 coupled CH_4 -Fe-Mn-S cycling (Slomp et al., 2013; Riedinger et al., 2014; Leu et al., 2020).
35 Microbial Fe-Mn-driven AOM contributes to the global consumption of CH_4 in marine
36 sediments in addition to sulfate (SO_4^{2-}), nitrite (NO_2^-), and nitrate (NO_3^-)-driven AOM
37 (Raghoebarsing et al., 2006; Beal et al., 2009; Knittel et al., 2009; Ettwig et al., 2010; Riedinger
38 et al., 2014; Xiao et al., 2023). A potential syntrophic coupling of AOM and reduction of Fe-
39 Mn-(oxyhydr)oxides in marine sediments was first inferred from incubation experiments using
40 ^{13}C -labeled CH_4 (Beal et al., 2009). The coupling of AOM and Fe-Mn-reduction is potentially
41 attributed to the activities of methanotrophs (ANME-1, ANME-3) and metal-reducing bacteria
42 (Beal et al., 2009; Oni et al., 2015), while Fe-Mn-(oxyhydr)oxide reduction may also be carried
43 out by ANME-2a, ANME-2c, and ANME-2d using multiheme cytochromes without syntrophic
44 metal-reducing bacterial partners (Ettwig et al., 2016; Scheller et al., 2016; Cai et al., 2018;
45 Leu et al., 2020). Plausible electron transport pathways coupling AOM and metal oxide
46 reduction include (a) direct electron transfer via microbial contact; (b) indirect electron transfer
47 by electron shuttling; (c) indirect electron transfer by a metal chelate; and (d) direct electron



48 transfer by nanowires (Folgosá et al., 2015; Wegener et al., 2015; He et al., 2018). The
49 biogeochemical reactions during Fe-Mn-AOM (Eq. 1 and 2) result in the mutual consumption
50 of CH₄ and Fe-Mn-(oxyhydr)oxides coupled with the enrichment of Fe²⁺ and Mn²⁺ in the
51 interstitial waters (Beal et al., 2009; Riedinger et al., 2014). Although SO₄²⁻-AOM (Eq. 3) is
52 responsible for > 90% of global methane consumption, Fe-Mn-AOM is thermodynamically
53 more favorable than SO₄²⁻-AOM (Beal et al., 2009) as evident from the ΔG values (Eq. 1, 2
54 and 3). The global predominance of SO₄²⁻-AOM may be attributed to its kinetics (Lovley and
55 Phillips, 1987).

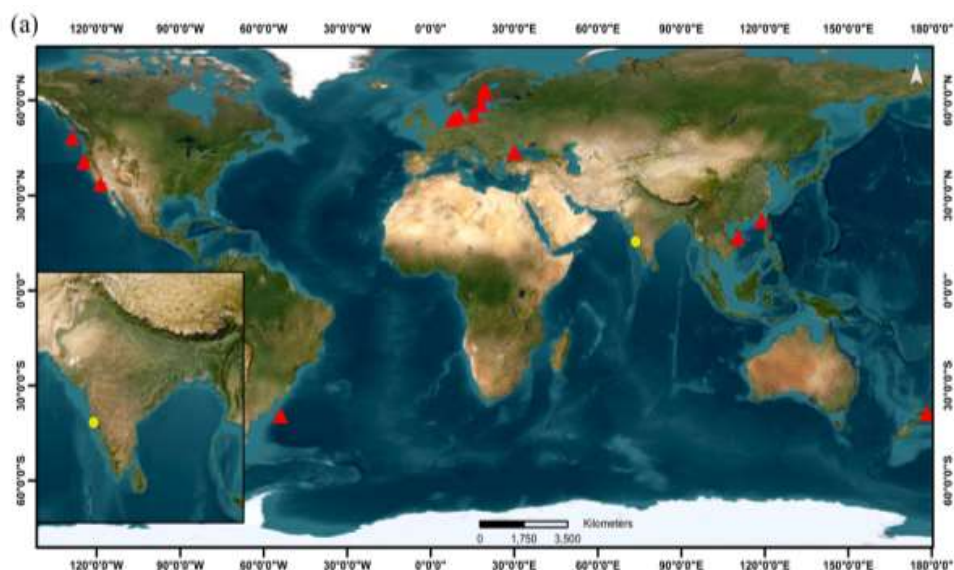


59 The availability of reactive Fe-Mn-(oxyhydr)oxides and low to undetectable SO₄²⁻
60 concentrations are considered essential geochemical conditions to drive Fe-Mn-AOM (Beal et
61 al., 2009; Oni et al., 2015; Aromokeye et al., 2019), however, a recent report (Li et al., 2019)
62 has shown the feasibility of Fe-Mn-AOM in SO₄²⁻-rich porewaters. The kinetics of Fe-Mn-
63 AOM depend on the content and composition of particulate Fe-Mn-(oxyhydr)oxides and
64 soluble ferric-organo complexes (e.g., ferric citrate) (Ettwig et al., 2016). It is observed that the
65 soluble metal complexes and ferrihydrite have higher bioavailability and AOM activity than
66 other solid metal-(oxyhydr)oxides (Lovley and Phillips, 1987; Norði et al., 2013; Ettwig et al.,
67 2016; Scheller et al., 2016). However, several incubation experiments and cultures have shown
68 that crystalline goethite, hematite, and magnetite can also serve as significant electron
69 acceptors for Fe-AOM (Bar-Or et al., 2017; Aromokeye et al., 2019; Li et al., 2021).

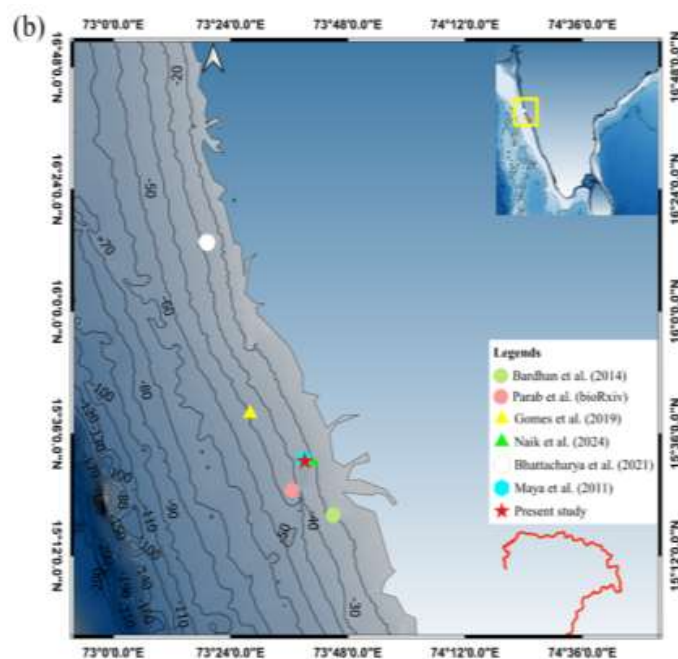
70 The global distribution of Fe-Mn-AOM is plotted in Figure 1a. Here, we present the first tell-
71 tale evidence of Fe-Mn-AOM from a seasonally hypoxic shelf zone. The study was carried out



72 in a sediment core (SSD070/7/GC6) collected off the west coast of India (WCI) at a water
73 depth of 28.5 m (Figure 1b). The seasonal hypoxic zone off the WCI covers an area of 1,80,000
74 km² and is the largest of all coastal hypoxic systems (Naqvi et al., 2000). The hypoxia is
75 attributed to the upwelling of cold, nutrient-rich waters onto the shelf region during July to
76 September, associated with the southwest monsoon. During the southwest monsoon, the WCI
77 receives substantial terrestrial as well as marine organic matter due to enhanced land runoff
78 and upwelling-driven marine productivity respectively. In contrast, during northeast monsoon,
79 the WCI experiences downwelling from November to April resulting in the prevalence of oxic
80 and oligotrophic conditions in the water column (Naqvi et al., 2000; Schott et al., 2001).
81 Consequently, the region exhibits contrasting seasonal biogeochemical conditions including
82 hydrographic and depositional features (Naqvi et al., 2006; Mazumdar et al., 2012). In the
83 present study, we have investigated possible driving factors fueling Fe-Mn-AOM activity in a
84 seasonally hypoxic shelf zone characterized by contrasting redox and depositional conditions.



85



86

87 **Figure 1.** a) Global map showing various study locations (red-filled triangles) with reported Fe-Mn-
88 AOM activities. The yellow-filled circle represents the present study location. The references are listed
89 in the supplementary material. (b) Map showing locations of the present study (SSD070/7/GC6) along
90 with those collected in previous studies (Maya et al., 2011; Bardhan et al., 2014; Gomes et al., 2019;
91 Bhattacharya et al., 2021; Naik et al., 2023; Parab et al., *bioRxiv*) from the inner shelf off the West Coast
92 of India (WCI). The red star represents the present study location (SSD070/7/GC6), while other colored
93 symbols represent locations in the WCI where $\delta^{13}\text{C}$ and $\delta^{15}\text{N}$ of suspended particulate organic matter
94 and microbiological studies have been conducted.

95

96

97

98



99 **2 Methodology**

100 **2.1 Onboard Sampling**

101 The studied gravity core (SSD070/7/GC6, 5.25 m long) was collected onboard ORV *Sindhu*
102 *Sadhana* in February 2020. The coring operation was carried out off Goa (latitude: 15.50985°N,
103 longitude: 73.65313°E) from the seasonal hypoxic coastal zone of the Eastern Arabian Sea.
104 Immediately after recovery, the core was subsampled onboard for hydrocarbon gas analysis
105 and porewater extraction.

106 For headspace methane analysis, the sediment was extracted using 50 ml cut syringes at an
107 interval of 10 cm and transferred into 20 ml headspace vials filled with 3 ml of KOH and 3 ml
108 of NaN₃ to trap CO₂ and arrest microbial activities respectively. The vials were flushed with
109 helium, homogenized, and stored at 4°C after sealing with butyl rubber septa. The core was
110 subsampled onboard for porewater extraction at 10 cm intervals and transferred into 50 ml
111 tarsons centrifuge vials using a 50 ml cut syringe under a stream of argon gas to avoid oxidation
112 of dissolved sulfide. The samples were centrifuged at 7000 rpm for 20 minutes in a Remi C-30
113 centrifuge. The supernatant porewater was filtered through a 0.2 µm Whatman syringe filter.
114 The filtered porewater was then stored in crimp vials under a helium head and subsequently
115 preserved at 4°C for measurement of various constituents. For dissolved sulfide ($\Sigma\text{HS}^- = \text{H}_2\text{S}$
116 $+ \text{HS}^- + \text{S}^{2-}$) analysis, 1 ml of 1 M CdNO₃ was added to fix all sulfides present as CdS.
117 Porewater samples for trace metal analysis were acidified with a known amount of concentrated
118 supra-pure HNO₃. All porewater samples were immediately crimp-sealed under a helium head
119 and stored at 4 °C until shore-based analysis. The core was subsampled for solid phase analysis
120 at 1 cm resolution and stored at 4 °C for further analysis.

121

122



123 **2.2 Porewater and headspace gas analysis**

124 The headspace hydrocarbon gas concentrations were determined using a trace GC equipped
125 with a flame ionization detector. Methane concentration measurements were carried out using
126 an external calibration line prepared from six different gas mixtures (CH₄, C₂H₆, C₃H₈, C₄H₁₀,
127 iso-C₄H₁₀, and CO₂) standards with concentrations varying from 10-1000 ppm. The carbon
128 isotopic composition of methane was determined using an isotope ratio mass spectrometer
129 (Thermo-Delta V plus) coupled with a gas chromatograph (Thermo-Trace GC Ultra). The
130 carbon isotope ratios of methane ($\delta^{13}\text{C}_{\text{CH}_4}$) are reported in delta notation as permil deviation
131 from Vienna Pee Dee Belemnite (VPDB) standard, and the external precision calculated for
132 the measurement is typically 0.07–0.09%. The concentration of dissolved inorganic carbon
133 (DIC) was measured using a carbon coulometer (UIC-CM5130) with ultrapure CaCO₃ as
134 standard. The measurement yielded a sample reproducibility of ± 0.3 %. The carbon isotope
135 ratios of DIC ($\delta^{13}\text{C}_{\text{DIC}}$) were analyzed using a Thermo Delta V continuous flow isotope ratio
136 mass spectrometer coupled with a GASBENCH II equipped with a PAL auto-sampler,
137 following Torres et al. (2005) and Peketi et al. (2020). Reference materials NBS-18, NBS-19,
138 Carrara marble standards, and in-house laboratory standards (MERCK high purity CaCO₃ and
139 Carbonate reference standard) were measured multiple times during the analysis with each
140 batch. The carbon isotope composition of DIC is reported in delta notation as permil deviation
141 from the VPDB standard. The measurement yielded a sample reproducibility of ± 0.02 %.
142 Porewater samples were diluted 40-fold for the determination of trace metals using high-
143 resolution inductively coupled plasma–mass spectrometry (Nu-ATTOM ES). NASS-5
144 (Seawater-certified reference material) and CASS-6 (Near Shore Seawater reference material)
145 were analyzed to check the accuracy and reproducibility of the sample analysis. The analytical
146 precision was monitored by repeated measurements of sample/standard and the calculated RSD
147 was less than 3%.



148 The porewater sulfate concentration was measured from the ΣHS^- free supernatant solution
149 using a Metrohm ion chromatograph (Basic IC plus 883) equipped with a suppressed
150 conductivity detector (Metrohm, IC detector 1.850.9010). A mixed solution of 1 mM NaHCO_3
151 and 3.2 mM Na_2CO_3 was used as the eluent, and 0.2 N H_2SO_4 was used as the suppressor
152 regeneration fluid. The samples were diluted 1000-fold with 18 M Ω ultrapure water prior to
153 analysis. The calibration line was prepared using a standard IC sulfate solution from a 100-
154 ppm mixed anion standard (Fluka), and the sample reproducibility was $\pm 0.1\%$. Quantification
155 of dissolved sulfide (ΣHS^-) was carried out following the methylene blue method (Cline et al.,
156 1969). Absorbance was measured at 670 nm on a spectrophotometer (Chemito Spectrascan
157 UV-2700). Sodium sulfide nonahydrate ($\geq 99.99\%$ purity, Merck) was used for the preparation
158 of calibration standards. The analytical error based on replicate standard measurements was <
159 3%.

160 **2.3 Solid phase analysis**

161 Iron extractions were conducted under anaerobic conditions using frozen sediment samples
162 following ascorbate and sodium dithionite steps. The leaching solutions were nitrogen-flushed
163 before extraction. The iron concentrations in ascorbate leached fraction (Fe_{Asc}) were
164 determined following previous studies (Hyacinthe et al., 2006; Raiswell et al., 2010) using
165 Atomic Absorption Spectrometer (Agilent-240AA) using air-acetylene flame. The sample
166 reproducibility for replicate analysis was within 5 %. The Fe_{Asc} free sediment residue was
167 leached for 2 hrs using sodium dithionite buffer for determination of dithionite extractable iron
168 (Fe_{D}) content following previous works (Mehra and Jackson, 1960; Canfield et al., 1989;
169 Volvaikar et al., 2020). The Fe_{D} content was determined using ferrozine-complexometry
170 technique on a Chemito spectrophotometer (Spectroscan UV 2700). The calibration line was
171 prepared from pure ferrous ammonium sulfate (Merck) and absorbance was measured at 515
172 nm. The replicate for Fe_{D} analysis yielded sample reproducibility within 6 %. The total



173 inorganic carbon content was measured using a UIC carbon coulometer (CM 5130). Ultrapure
174 CaCO_3 from Sigma-Aldrich was used as a standard reference material for measurement
175 (Carbon content: $12.0 \pm 0.25\%$). The measurement of total carbon (TC) content was carried out
176 on freeze-dried and desalinated samples using an EA1112 elemental analyzer (Thermo Fisher
177 Scientific, Germany). The total organic carbon (TOC) content (Figure S2; Table S2) was
178 calculated by subtracting TIC from TC. NC soil was used as a calibration standard for TC. The
179 reproducibility for TC in soil standards B2184 and B2152 was found to be $2.11 + 0.1 \%$ and
180 $1.53 + 0.07 \%$ respectively. The carbon and nitrogen isotope ratio of TOC ($\delta^{13}\text{C}_{\text{TOC}}$) and
181 nitrogen ($\delta^{15}\text{N}$) were measured on decarbonated samples using a Delta-V-plus isotope ratio
182 mass spectrometer coupled with an elemental analyzer (Thermo Flash EA 2000). The carbon
183 and nitrogen isotope ratios are reported as per mil (‰) deviations from the isotopic composition
184 of VPDB and atmospheric N_2 with reproducibility better than $\pm 0.3\%$.

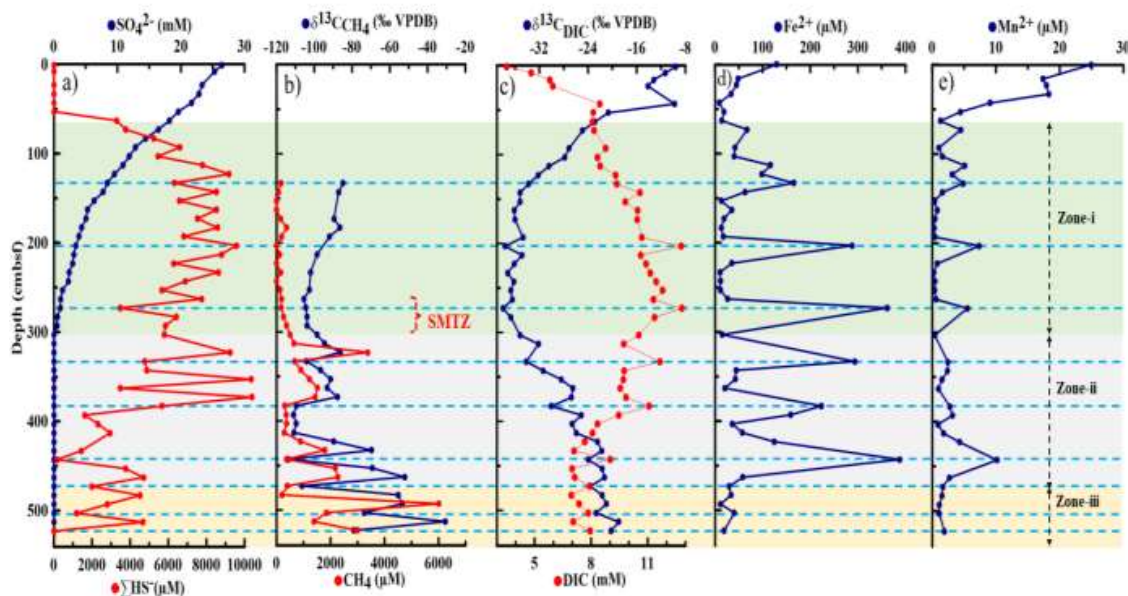
185 **3 Results and Discussion**

186 **3.1 Evidence for SO_4^{2-} and Fe-Mn-AOM**

187 Based on the porewater SO_4^{2-} and Fe-Mn concentration profiles (Figures 2a-2e; Table S1), the
188 sediment core can be divided into three distinctive diagenetic regimes (zone-i, zone-ii, and
189 zone-iii). Zone-i (63 to 303 cmbsf) is characterized by Fe^{2+} and Mn^{2+} enrichment (Fe^{2+} : 10.75
190 to $361.3 \mu\text{M}$ and Mn^{2+} : 0.28 to $7.39 \mu\text{M}$) at high SO_4^{2-} concentrations (0.5 to 18.2 mM); zone-
191 ii (303 to 463 cmbsf) is characterized by SO_4^{2-} depletion (0.4 to $1.45 \mu\text{M}$) coupled with Fe^{2+}
192 and Mn^{2+} enrichment (Fe^{2+} : 14.9 to $387.5 \mu\text{M}$ and Mn^{2+} : 0.41 to $10.17 \mu\text{M}$); and zone-iii (463-
193 523 cmbsf) shows SO_4^{2-} depletion (below detection limit to $0.8 \mu\text{M}$) coupled with depleted Fe^{2+}
194 and Mn^{2+} concentrations (Fe^{2+} : 11.85 to $58.2 \mu\text{M}$ and Mn^{2+} : 1.13 to $2.68 \mu\text{M}$). The ΣHS^-
195 concentrations remain consistently high (163 to $10,385 \mu\text{M}$) below 63 cm from the seabed.

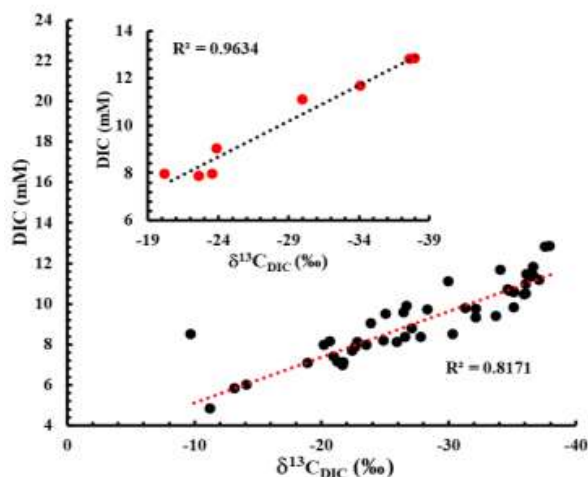


196 The SMTZ is identified within an approximate depth window of 263 to 303 cmbsf (Figures 2a
197 and 2b). Within the SMTZ, AOM activity is identified by simultaneous depletion in CH₄
198 concentrations (188.9 to 503.2 μM) and C-isotope ratios of CH₄ ($\delta^{13}\text{C}_{\text{CH}_4}$: -105.6 to -98.6 ‰)
199 and DIC ($\delta^{13}\text{C}_{\text{DIC}}$: -38 to 35.2 ‰). The AOM-driven depletion in $\delta^{13}\text{C}_{\text{CH}_4}$ and $\delta^{13}\text{C}_{\text{DIC}}$ values
200 within the SMTZ may be attributed to (i) DIC back flux during AOM (Yoshinaga et al., 2014)
201 (ii) concurrent methanotrophic and methanogenic activity (Borowski et al., 1997), (iii) the
202 ability of ANMEs to perform as facultative methanogens (Pohlman et al., 2008), and (iv)
203 intracellular reaction reversibilities along enzymatic AOM pathway (Wegener et al., 2021).
204 Above SMTZ, the upward increasing trend in $\delta^{13}\text{C}_{\text{CH}_4}$ values may be attributed to ¹³C
205 enrichment (Figure 2b; Alperin et al., 1988; Whiticar et al., 1996; Martens et al., 1999;
206 Whiticar, 1999) in the residual methane (kinetic isotope effect) due to methane oxidation and
207 lack of carbon recycling at high SO₄²⁻ concentrations (SO₄²⁻>0.5 mM; Yoshinaga et al., 2014;
208 Wegener et al., 2021). Below the SMTZ, the methanogenesis trend is superimposed by depths
209 of intermittent AOM activity evident from depletion in CH₄ concentrations (1.04 to 4.19 mM)
210 coupled with a sharp decrease in $\delta^{13}\text{C}_{\text{CH}_4}$ (-17.95 to -61 ‰) and $\delta^{13}\text{C}_{\text{DIC}}$ values (-1.8 to -4.1
211 ‰) and increase in DIC concentrations (1 to 2.7 mM). The cross plot of DIC concentrations vs
212 $\delta^{13}\text{C}_{\text{DIC}}$ values for the overall core and the Fe-Mn-AOM specific points show negative
213 correlations (Figure 3). The intermittent increase in DIC concentrations and decrease in $\delta^{13}\text{C}_{\text{DIC}}$
214 values can also be identified within the sulfatic zone-i.



215

216 **Figure 2.** Figure showing Fe-Mn-AOM and SO_4^{2-} -AOM activities by means of pore fluid
 217 chemistry in seasonally hypoxic coastal sediment of the Eastern Arabian Sea. (a) Porewater SO_4^{2-}
 218 (mM) and ΣHS^- (μM) concentrations. (b) Dissolved CH_4 concentrations (μM) and $\delta^{13}\text{C}_{\text{CH}_4}$ values.
 219 (c) Dissolved DIC concentrations (mM) and $\delta^{13}\text{C}_{\text{DIC}}$ values (d, e) Dissolved Fe and Mn (μM)
 220 concentrations. The blue dashed lines represent the depth layers with AOM activities. The red curly
 221 bracket depicts SMTZ. The different color shades represent zone-i, zone-ii, and zone-iii.



222

223 **Figure 3.** Cross plot of DIC concentration (mM) vs $\delta^{13}\text{C}_{\text{DIC}}$ (‰) values in the studied sediment core
224 (represented by black dots with an R^2 value of 0.82). The inset cross plot of DIC vs. $\delta^{13}\text{C}_{\text{DIC}}$ (represented
225 by red dots with an R^2 value of 0.96) corresponds to values specific to Fe-Mn-AOM (marked by blue
226 dashed lines in Figure 2).

227 The most intriguing observation of the present study is the intermittent increase in porewater
228 Fe^{2+} and Mn^{2+} concentrations (Figures 2d & 2e). Within zone-i and ii, the marked increase in
229 porewater Fe^{2+} and Mn^{2+} concentrations are associated with AOM activities. However, in zone-
230 iii, the AOM activities are not associated with significant porewater Fe^{2+} and Mn^{2+} enrichment.

231 The porewater SO_4^{2-} , Fe^{2+} , Mn^{2+} , CH_4 , and DIC concentrations along with $\delta^{13}\text{C}_{\text{CH}_4}$ and $\delta^{13}\text{C}_{\text{DIC}}$
232 depth profiles provide tell-tale evidence of both SO_4^{2-} -AOM and Fe-Mn-AOM in the present
233 study. Zonation of the geochemical profiles shows co-occurrence of SO_4^{2-} -AOM and Fe-Mn-
234 AOM in zone-i, and Fe-Mn-AOM in zone-ii and iii. The occurrence of Fe-Mn-AOM in SO_4^{2-} -
235 rich zone has also been reported in an earlier study from the Dongsha area, South China Sea
236 (Li et al., 2019). These observations are further supported by an incubation study (Segarra et
237 al., 2013) where notable rates of Fe-Mn-AOM coincide with comparatively elevated levels of



238 SO_4^{2-} -AOM. Within zone-ii, where SO_4^{2-} concentrations are reduced to 0.4 to 1.45 μM , the
239 Fe^{2+} and Mn^{2+} concentration spikes may be attributed primarily to Fe-Mn-(oxyhydr)oxides
240 fueling AOM activity (Riedinger et al., 2014; Egger et al., 2015; Egger et al., 2017).

241 In most of the previous studies (Crowe et al., 2009; Sivan et al., 2011; Slomp et al., 2013;
242 Riedinger et al., 2014; Egger et al., 2015; Egger et al., 2016a; Egger et al., 2016b; Egger et al.,
243 2017; Aromokeye et al., 2019; Vigderovich et al., 2019; Luo et al., 2020; Xiao et al., 2023),
244 AOM-driven Fe^{2+} - Mn^{2+} enrichment has been reported at low to negligible ΣHS^- concentrations
245 (Figure S1). However, the present study demonstrates tell-tale signatures of substantially high
246 porewater Fe^{2+} - Mn^{2+} concentrations despite high ΣHS^- concentrations. A similar observation
247 was also reported in previous studies (Ramírez-Pérez et al., 2015; Li et al., 2019). Equation-1
248 shows that for every mole of DIC produced via Fe-AOM, 8 moles of Fe^{2+} are produced. The
249 DIC concentration perturbations (along the blue dashed lines) may be converted to equivalent
250 μM of Fe^{2+} produced via Fe^{3+} reduction in the pore waters. The stoichiometrically calculated
251 amount of Fe^{2+} produced ranges from 11673 μM to 17163 μM in zone-i-ii and 6192 to 8259
252 μM in zone-iii. The measured porewater Fe^{2+} concentrations are approximately 1.65-3% of the
253 calculated Fe^{2+} in zone-i-ii and 0.2-0.6 % in zone-iii. Thus, the measured Fe^{2+} concentration is
254 the residual Fe^{2+} left after sulfidization (FeS/FeS_2 : Hensen et al., 2003; Treude et al., 2014;
255 Peketi et al., 2015). Therefore, the lack of significant Fe^{2+} and Mn^{2+} enrichment in zone-iii may
256 indicate complete consumption of Fe^{2+} and Mn^{2+} via sulfidization.

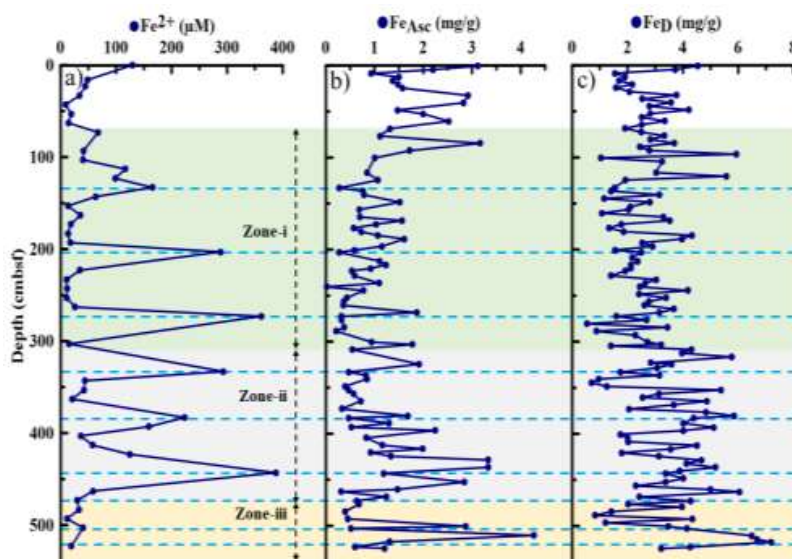
257 Additional processes that may enhance the metal concentrations in the sediment pore waters is
258 the presence of metal (Fe-Mn) sulfide colloids (Rickard et al., 2007) as nanoparticles.
259 Dissolution of porewater Fe-Mn sulfide nanoparticles (Morse et al., 1999; Olson et al., 2017)
260 in acid during sample preparation results in the simultaneous occurrence of Fe^{2+} and Mn^{2+}
261 spikes in porewater. However, if the observed Fe^{2+} - Mn^{2+} concentration spikes in this study are



262 merely an analytical artifact, then under the presence of such high dissolved sulfide
263 concentrations, Fe^{2+} - Mn^{2+} spikes would be expected at all depths. The absence of Fe-Mn spikes
264 corroborated with distinct increase in DIC concentration and decrease in $\delta^{13}\text{C}_{\text{DIC}}$ values rules
265 out such artifact generation.

266 **3.2 Possible limiting factors and focused Fe-Mn-AOM**

267 An essential prerequisite for Fe-Mn-AOM is the presence of appreciable quantities of Fe-Mn-
268 (oxyhydroxides) to react with CH_4 (Beal et al., 2009) as evident from the stoichiometric ratios
269 (Eq. 1). Results from iron extractions indicate the presence of significant amount of iron in
270 highly reactive/bioavailable (Fe_{Asc}) (Figure 4b) and dithionite extractable phases (Fe_{D}) (Figure
271 4c, Table S2). The Fe_{Asc} and Fe_{D} contents in the sediment range from 0.01 to 4.27 mg/g (Avg:
272 1.2 ± 0.86 mg/g) and 0.54 to 7.2 mg/g (Avg: 3.03 ± 1.36 mg/g) respectively. The porewater Fe^{2+}
273 concentration spikes are associated with marked depletion in Fe_{Asc} content, indicating
274 consumption of ferrihydrite and other bioavailable iron through Fe-AOM (Figure 4). However,
275 the presence of substantial content of both Fe_{D} and Fe_{Asc} throughout the core length suggests
276 Fe-AOM is not limited by reactive iron content. In the present study, the high reactive iron flux
277 in the shelf zone may be attributed to rapid sedimentation rates (150 to 1500 cm/ky) and fluvial
278 input from Fe-Mn-rich provenances (Fernandes et al., 2020). Additionally, the presence of CH_4
279 throughout the Fe-Mn-AOM zones suggests that neither CH_4 nor reactive Fe. are limiting
280 factors responsible for the focused occurrences of Fe-AOM in the sediment core.



281

282 **Figure 4.** Depth profiles of (a) Porewater Fe^{2+} concentrations (μM). (b) solid phase ascorbic acid
283 leachable iron (Fe_{Asc}) and (c) sodium dithionite leachable iron (Fe_{D}) contents (in mg/g). The blue dashed
284 lines represent the depth layers with AOM activities. The different color shades represent zone-i,
285 zone-ii, and zone-iii.

286 One of the plausible factors responsible for the occurrence of focused Fe-Mn-AOM in distinct
287 sediment layers could be the spatiotemporal enrichment of the microbial population driving
288 Fe-Mn-AOM. The latter in turn could be the result of the interplay between several
289 biogeochemical factors. For instance, the shallow shelf off WCI is highly dynamic,
290 experiencing drastic changes in water column redox conditions, marine productivity, fluvial
291 fluxes of organic matter, sediment load, and extensive denitrification (Naqvi et al., 2000; Schott
292 et al., 2001; Naqvi et al., 2006; Maya et al., 2011; Mazumdar et al., 2012; Fernandes et al.,
293 2020). A large range in TOC contents (1.45 to 31.3 mg/g), $(\text{TOC}/\text{TN})_{\text{molar}}$ ratios (3.47 to 27.32),
294 $\delta^{13}\text{C}_{\text{TOC}}$ (-20.69 to -25.93 ‰), and $\delta^{15}\text{N}$ values (-3.6 to 7.7 ‰) in the present and previous
295 studies (Mazumdar et al., 2012; Fernandes et al., 2020) indicate marked temporal variation in
296 the fluvial and marine organic matter fluxes and denitrification conditions in WCI (Figure S2,

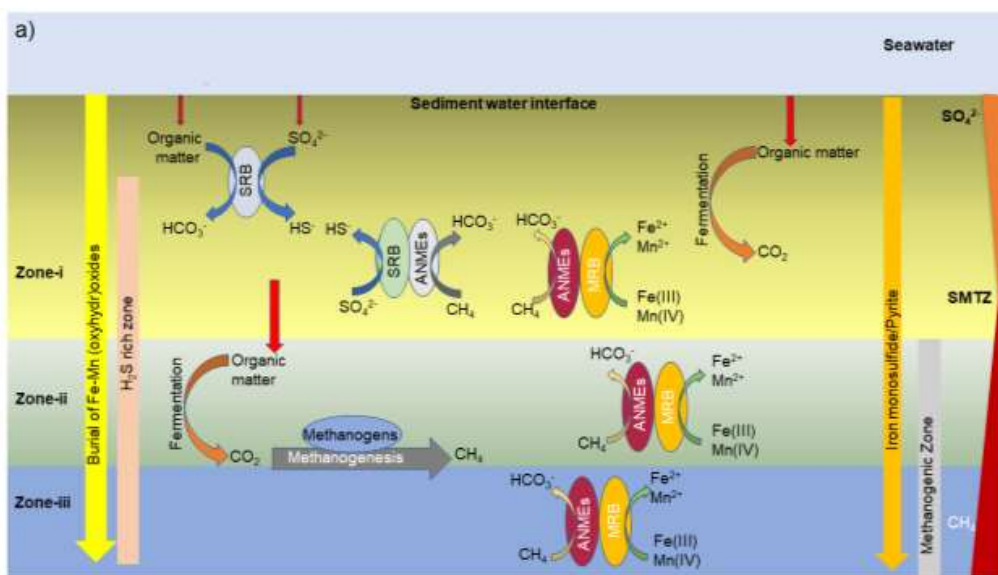


297 Table S2). Previous studies (near SSD070/7/GC6; Figure 1b) investigating carbon and nitrogen
298 stable isotopes of suspended particulate organic matter (SPOM) in the estuary (Bardhan et al.,
299 2014) and shelf zone (Maya et al., 2011) of WCI revealed significant intra-annual variations in
300 $\delta^{15}\text{N}$ (estuary: 0.69 to 7.26 ‰; shelf: -4.17 to 10.43 ‰) and $\delta^{13}\text{C}$ (estuary: -30.14 to -19.52 ‰,
301 shelf: -17.64 to -26.74 ‰) throughout the year. These variations reflect the complex and
302 dynamic nature of biogeochemical processes and organic matter sources in the coastal waters
303 of the WCI. Corroboratively, significant variations in the diversity, abundance, and activity of
304 microorganisms, attributable to seasonal differences in nutrient availability, have been recorded
305 in the water column between monsoon and non-monsoon seasons (Gomes et al., 2019; Naik et
306 al., 2024; Parab et al., *bioRxiv*). Spatiotemporally contrasting biogeochemical conditions of
307 shallow coastal waters have profound influence on the structure and function of underlying
308 sedimentary microbiomes (Bhattacharya et al., 2021). An earlier study (Orsi et al., 2017) from
309 the North Eastern Arabian Sea oxygen minimum zone reported stratigraphic microbial
310 distribution attributed to palaeoceanographic conditions. It was also proposed that focused
311 abundances of microbial communities in sediment layers are expected to be most pronounced
312 in the coastal region due to drastic variations in marine redox conditions and terrestrial fluxes.
313 In the context of the biogeochemical phenomenon revealed here, we hypothesize a dominant
314 role of the localized abundance of metal-reducing bacterial/archaeal communities in restricting
315 Fe-Mn-AOM activities into specific sedimentary strata. The focusing of microbial activity in
316 different sediment layers may be attributed to factors such as past environmental conditions
317 and depositional processes (Parkes et al., 2000; Orsi et al., 2017; Hoshino et al., 2020). Seasonal
318 coastal hypoxia coupled with a wide range of organic matter (marine to terrestrial) fluxes may
319 play important roles in stratigraphic microbial distributions and heterogeneity in
320 biogeochemical processes.



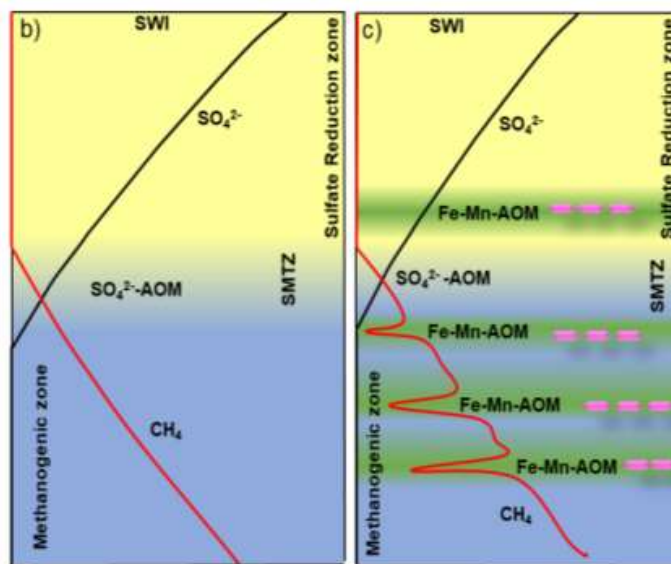
321 Our hypothesis is supported by metagenomic sequencing (Sarkar et al., *in prep*; Table S3)
322 carried out in a ~3 m long, sulfide-rich, sediment core (SSK42/9; water depth: 31 m; Figure
323 1b), collected from a nearby shallow coastal site (Bhattacharya et al., 2021) which shows the
324 presence of two species-level entities affiliated to the uncultivated archaeon
325 *Candidatus Methanoperedens* (GenBank assembly numbers GCA_003104905.1 and
326 GCA_001317315.1) reported thus far for potential abilities to harness anaerobic methane
327 oxidation to the reduction of Fe (III) (Ettwig et al., 2016; Cai et al., 2018). However, the final
328 microbiological corroboration of the focused Fe-Mn-AOM phenomenon hinges on the future
329 enrichment of the genome sequence database for microorganisms having definite and complete
330 Fe-Mn-AOM attributes.

331 Being the world's largest coastal hypoxic zone covering an area of 0.18 million sq. km, the net
332 influence of Fe-Mn-AOM could be significant in sedimentary methane consumption. A
333 schematic representation of CH₄-S-Fe-Mn cycling in coastal hypoxic sediments of the Eastern
334 Arabian Sea is presented in Figures 5a, 5b and 5c respectively.



335

SRB: Sulfate reducing bacteria; MRB: Metal reducing bacteria; ANME: Anaerobic methanotrophic archaea



336

SMTZ: Sulfate methane transition zone
SWI: Sediment water interface

Localization of Fe-Mn reducing microbial communities

337 **Figure 5.** (a) Schematic representation of Fe-Mn-AOM and SO_4^{2-} -AOM activities within the sediment

338 column. The figure depicts different zonation within the sediment column, showing the co-occurrence

339 of SO_4^{2-} -AOM and Fe-Mn-AOM in zone-i and Fe-Mn-AOM in zone-ii-iii. Schematic representation of



340 pore fluid vertical profiles in the absence (b) and presence (c) of Fe-Mn-AOM activity. The green-
341 shaded regions in the methanogenic zone represent potential Fe-Mn-AOM depth layers, controlled by
342 the localization of metal-reducing microbial communities.

343 **4 Conclusions**

344 The comprehensive geochemical investigation of the sediment core (5.25 m) retrieved from the
345 seasonally hypoxic shelf sediment off the eastern Arabian Sea (west coast of India) has
346 unveiled compelling evidence of focused Fe-Mn-AOM occurring at multiple depths beneath
347 the seafloor. The accumulation of porewater Fe^{2+} and Mn^{2+} despite elevated concentrations of
348 ΣHS^- , suggests the predominant production of Fe^{2+} and Mn^{2+} rather than consumption through
349 metal sulfidization processes. This study demonstrates that Fe-Mn-AOM remains a significant
350 biogeochemical phenomenon even within SO_4^{2-} and ΣHS^- -rich sediments. Our findings are also
351 relevant in assessing the consumption of CH_4 , a greenhouse gas in organic-rich coastal
352 sediments, thus having implications for climate change research. This study presents a new
353 perspective by documenting the biogeochemical heterogeneity in the occurrence of Fe-Mn-
354 AOM, possibly attributed to deposition-controlled Fe-Mn reducing microbial population
355 distribution in a highly dynamic coastal environment sensitive to climate change. The findings
356 of the present study may have a far-reaching influence on coupled CH_4 -Mn-Fe-S cycling in
357 expanding hypoxic coastal regions of the global ocean. Our findings lead to a hypothesis that
358 necessitates future examination of microbial communities in seasonally hypoxic sediments and
359 SPOM at high depth and temporal resolution which may uncover the complex interactions
360 between microbial life and their environment.

361 **Appendices:** No appendix is there in this manuscript.

362 **Code Availability:** No code was used in this manuscript.

363 **Data availability:** All the data used in this study is incorporated in the supplementary text as
364 table S1, table S2 and table S3.



365 **Sample availability:** Samples are available with the author.

366 **Video supplement:** No video component is there in this manuscript.

367 **Author Contributions:** K.S., A.P., and A.M. designed the research; A.M. obtained the funding;

368 K.S., A.Z., and S.P.K.P. analyzed the data; A.G., M.S., and J.M. carried out sampling; and K.S.,

369 A.P., and A.M. wrote the paper.

370 **Competing interests:** The authors declare that they have no conflict of interest.

371 **Acknowledgments**

372 The authors thank the Director of CSIR-NIO for supporting this study. We sincerely thank the

373 Ministry of Earth Sciences (GAP2303) for funding the program and the Council of Scientific

374 and Industrial Research (CSIR) for providing a research fellowship to K.S. We are grateful to

375 Dr. V.V.S.S. Sarma for helping with carbon and nitrogen isotopic measurements. We also

376 thank Dr. Wriddhiman Ghosh for his valuable suggestions on the manuscript. Sincere thanks

377 to Mr. Sidharth Vernekar, Mr. Harish Kumar, and crewmembers for onboard support. Thanks

378 are due to Mr. Robin John and Mrs. Teja Naik for helping with HR-ICPMS and carbon

379 coulometry analysis.

380 **References**

381 Alperin, M. J., Reeburgh, W. S., and Whiticar, M. J.: Carbon and hydrogen isotope

382 fractionation resulting from anaerobic methane oxidation, *Global biogeochemical cycles*, 2,

383 279-288, <https://doi.org/10.1029/GB002i003p00279>, 1988.

384

385 Aromokeye, D. A., Kulkarni, A. C., Elvert, M., Wegener, G., Henkel, S., Coffinet, S.,

386 Eickhorst, T., Oni, O. E., Richter-Heitmann, T., and Schnakenberg, A.: Rates and microbial

387 players of iron-driven anaerobic oxidation of methane in methanic marine sediments, *Frontiers*

388 in Microbiology, 10, 3041, <https://doi.org/10.3389/fmicb.2019.03041>, 2019.

389



390 Bardhan, P., Karapurkar, S. G., Shenoy, D. M., Kurian, S., Sarkar, A., Maya, M. V., Naik, H.,
391 Varik, S., and Naqvi, S. W. A.: Carbon and nitrogen isotopic composition of suspended
392 particulate organic matter in Zuari Estuary, west coast of India, *Journal of Marine Systems*,
393 141, 90-97, <https://doi.org/10.1016/j.jmarsys.2014.07.009>, 2014.

394

395 Bar-Or, I., Elvert, M., Eckert, W., Kushmaro, A., Vigderovich, H., Zhu, Q., Ben-Dov, E., and
396 Sivan, O.: Iron-coupled anaerobic oxidation of methane performed by a mixed bacterial-
397 archaeal community based on poorly reactive minerals, *Environmental science & technology*,
398 51, 12293-12301, <https://doi.org/10.1021/acs.est.7b03126>, 2017.

399

400 Beal, E. J., House, C. H., and Orphan, V. J.: Manganese-and iron-dependent marine methane
401 oxidation, *Science*, 325, 184-187, <https://doi.org/10.1126/science.1169984>, 2009.

402

403 Bhattacharya, S., Mapder, T., Fernandes, S., Roy, C., Sarkar, J., Rameez, M. J., Mandal, S.,
404 Sar, A., Chakraborty, A. K., and Mondal, N.: Sedimentation rate and organic matter dynamics
405 shape microbiomes across a continental margin, *Biogeosciences*, 18, 5203-5222,
406 <https://doi.org/10.5194/bg-18-5203-2021>, 2021.

407

408 Borowski, W. S., Paull, C. K., and Ussler III, W.: Carbon cycling within the upper
409 methanogenic zone of continental rise sediments: An example from the methane-rich sediments
410 overlying the Blake Ridge gas hydrate deposits., *Marine Chemistry*, 57, 299-311,
411 [https://doi.org/10.1016/S0304-4203\(97\)00019-4](https://doi.org/10.1016/S0304-4203(97)00019-4), 1997.

412

413 Cai, C., Leu, A. O., Xie, G.-J., Guo, J., Feng, Y., Zhao, J.-X., Tyson, G. W., Yuan, Z., and Hu,
414 S.: A methanotrophic archaeon couples anaerobic oxidation of methane to Fe (III) reduction,
415 *The ISME Journal*, 12, 1929-1939, <https://doi.org/10.1038/s41396-018-0109-x>, 2018.

416

417 Canfield, D.: Reactive iron in marine sediments, *Geochimica et Cosmochimica Acta*, 53, 619-
418 632, [https://doi.org/10.1016/0016-7037\(89\)90005-7](https://doi.org/10.1016/0016-7037(89)90005-7), 1989.

419

420 Cline, J. D.: Spectrophotometric determination of hydrogen sulfide in natural waters,
421 *Limnology and oceanography*, 14, 454-458, <https://doi.org/10.4319/lo.1969.14.3.0454>, 1969.

422



423 Crowe, S. A., Katsev, S., Leslie, K., Sturm, A., Magen, C., Nomosatryo, S., Pack, M. A.,
424 Kessler, J. D., Reeburgh, W. S., and Roberts, J. A.: The methane cycle in ferruginous Lake
425 Matano, *Geobiology*, 9, 61-78, <https://doi.org/10.1111/j.1472-4669.2010.00257.x>, 2011.

426

427 Egger, M., Rasigraf, O., Sapart, C. J., Jilbert, T., Jetten, M. S. M., Rockmann, T., Van der
428 Veen, C., Banda, N., Kartal, B., and Ettwig, K. F.: Iron-mediated anaerobic oxidation of
429 methane in brackish coastal sediments, *Environmental science & technology*, 49, 277-283,
430 <https://doi.org/10.1021/es503663z>, 2015.

431

432 Egger, M., Lenstra, W., Jong, D., Meysman, F. J. R., Sapart, C. I. J., Van der Veen, C.,
433 Röckmann, T., Gonzalez, S., and Slomp, C. P.: Rapid sediment accumulation results in high
434 methane effluxes from coastal sediments, *PloS one*, 11, e0161609,
435 <https://doi.org/10.1371/journal.pone.0161609>, 2016a.

436

437 Egger, M., Kraal, P., Jilbert, T., Sulu-Gambari, F., Sapart, C. J., Röckmann, T., and Slomp, C.
438 P.: Anaerobic oxidation of methane alters sediment records of sulfur, iron and phosphorus in
439 the Black Sea, *Biogeosciences*, <https://doi.org/10.5194/bg-13-5333-2016>, 2016b.

440

441 Egger, M., Hagens, M., Sapart, C. I. J., Dijkstra, N., van Helmond, N. A. G. M., Mogollán, J.
442 M., Risgaard-Petersen, N., van der Veen, C., Kasten, S., and Riedinger, N.: Iron oxide
443 reduction in methane-rich deep Baltic Sea sediments, *Geochimica et Cosmochimica Acta*, 207,
444 256-276, <https://doi.org/10.1016/j.gca.2017.03.019>, 2017.

445

446 Ettwig, K. F., Butler, M. K., Le Paslier, D., Pelletier, E., Mangenot, S., Kuypers, M. M. M.,
447 Schreiber, F., Dutilh, B. E., Zedelius, J., and de Beer, D.: Nitrite-driven anaerobic methane
448 oxidation by oxygenic bacteria, *Nature*, 464, 543-548, <https://doi.org/10.1038/nature08883>,
449 2010.

450

451 Ettwig, K. F., Zhu, B., Speth, D., Keltjens, J. T., Jetten, M. S. M., and Kartal, B.: Archaea
452 catalyze iron-dependent anaerobic oxidation of methane, *Proceedings of the National Academy
453 of Sciences of the United States of America*, 113, 12792-12796, <https://doi.org/10.1073/pnas.1609534113>, 2016.

454
455



456 Fernandes, S., Mazumdar, A., Peketi, A., Anand, S. S., Rengarajan, R., Jose, A., Manaskanya,
457 A., Carvalho, M. A., and Shetty, D.: Sulfidization processes in seasonally hypoxic shelf
458 sediments: a study off the West coast of India, *Marine and Petroleum Geology*, 117, 104353,
459 <https://doi.org/10.1016/j.marpetgeo.2020.104353>, 2020.

460

461 Folgosa, F., Tavares, P., and Pereira, A. S.: Iron management and production of electricity by
462 microorganisms, *Applied microbiology and biotechnology*, 99, 8329-8336,
463 <https://doi.org/10.1007/s00253-015-6897-2>, 2015.

464

465 Gomes, J., Khandeparker, R., Meena, R. M., and Ramaiah, N.: Bacterial community
466 composition markedly altered by coastal hypoxia, *Journal of Microbiology*, 59, 200-208,
467 <https://doi.org/10.1007/s12088-019-00790-5>, 2019.

468

469 He, Z., Zhang, Q., Feng, Y., Luo, H., Pan, X., and Gadd, G. M.: Microbiological and
470 environmental significance of metal-dependent anaerobic oxidation of methane, *Science of
471 Total Environment*, 610, 759-768, <https://doi.org/10.1016/j.scitotenv.2017.08.140>, 2018.

472

473 Hensen, C., Zabel, M., Pfeifer, K., Schwenk, T., Kasten, S., Riedinger, N., Schulz, H., and
474 Boetius, A.: Control of sulfate pore-water profiles by sedimentary events and the significance
475 of anaerobic oxidation of methane for the burial of sulfur in marine sediments, *Geochimica et
476 Cosmochimica Acta*, 67, 2631-2647, [https://doi.org/10.1016/S0016-7037\(03\)00199-6](https://doi.org/10.1016/S0016-7037(03)00199-6), 2003.

477

478 Hoshino, T., Doi, H., Uramoto, G.-I., Wörmer, L., Adhikari, R. R., Xiao, N., Morono, Y., D'
479 Hondt, S., Hinrichs, K.-U., and Inagaki, F.: Global diversity of microbial communities in
480 marine sediment, *Proceedings of the National Academy of Sciences of the United States of
481 America*, 117, 27587-27597, <https://doi.org/10.1073/pnas.1919139117>, 2020.

482

483 Hyacinthe, C., Bonneville, S., and Van Cappellen, P.: Reactive iron (III) in sediments: chemical
484 versus microbial extractions, *Geochimica et Cosmochimica Acta*, 70, 4166-4180,
485 <https://doi.org/10.1016/j.gca.2006.05.018>, 2006.

486



487 Knittel, K. and Boetius, A.: Anaerobic oxidation of methane: progress with an unknown
488 process, *Annual review of microbiology*, 63, 311-334, <https://doi.org/10.1146/annurev.micro.61.080706.093130>, 2009.

490

491 Leu, A. O., Cai, C., McIlroy, S. J., Southam, G., Orphan, V. J., Yuan, Z., Hu, S., and Tyson,
492 G. W.: Anaerobic methane oxidation coupled to manganese reduction by members of the
493 *Methanoperedenaceae*, *The ISME journal*, 14, 1030-1041, <https://doi.org/10.1038/s41396-020-0590-x>, 2020.

495

496 Li, J., Li, L., Bai, S., Ta, K., Xu, H., Chen, S., Pan, J., Li, M., Du, M., and Peng, X.: New
497 insight into the biogeochemical cycling of methane, S and Fe above the Sulfate-Methane
498 Transition Zone in methane hydrate-bearing sediments: A case study in the Dongsha area,
499 South China Sea, *Deep Sea Research Part I: Oceanographic Research Papers*, 145, 97-108,
500 <https://doi.org/10.1016/j.dsr.2019.01.011>, 2019.

501

502 Li, W., Cai, C., Song, Y., Ni, G., Zhang, X., and Lu, P.: The role of crystalline iron oxides in
503 methane mitigation through anaerobic oxidation of methane, *ACS ES & T Water*, 1, 1153-
504 1160, <https://doi.org/10.1021/acsestwater.0c00199>, 2021.

505

506 Lovley, D. R. and Phillips, E. J. P.: Competitive mechanisms for inhibition of sulfate reduction
507 and methane production in the zone of ferric iron reduction in sediments, *Applied and
508 Environmental Microbiology*, 53, 2636-2641, <https://doi.org/10.1128/aem.53.11.26362641>.
509 1987, 1987.

510

511 Luo, M., Torres, M. E., Hong, W.-L., Pape, T., Fronzek, J., Kutterolf, S., Mountjoy, J. J., Orpin,
512 A., Henkel, S., and Huhn, K.: Impact of iron release by volcanic ash alteration on carbon
513 cycling in sediments of the northern Hikurangi margin, *Earth and Planetary Science Letters*,
514 541, 116288, <https://doi.org/10.1016/j.epsl.2020.116288>, 2020.

515

516 Martens, C., Albert, D., and Alperin, M.: Stable isotope tracing of anaerobic methane oxidation
517 in the gassy sediments of Eckernförde Bay, German Baltic Sea, *American Journal of Science*,
518 299, 589-610, <https://doi.org/10.2475/AJS.299.7-9.589>, 1999.

519



520 Maya, M. V., Karapurkar, S. G., Naik, H., Roy, R., Shenoy, D. M., and Naqvi, S. W. A.: Intra-
521 annual variability of carbon and nitrogen stable isotopes in suspended organic matter in waters
522 of the western continental shelf of India, *Biogeosciences*, 8, 3441-3456,
523 <https://doi.org/10.5194/bg-8-3441-2011>, 2011.

524

525 Mazumdar, A., Peketi, A., Joao, H., Dewangan, P., Borole, D. V., and Kocherla, M.:
526 Sulfidization in a shallow coastal depositional setting: Diagenetic and palaeoclimatic
527 implications, *Chemical Geology*, 322, 68-78, <https://doi.org/10.1016/j.chemgeo.2012.06.005>,
528 2012.

529

530 Mehra, O. and Jackson, M.: Iron oxide removal from soils and clays by a dithionite-citrate
531 system buffered with sodium bicarbonate, *Clays and clay Minerals*, 7, 317-327,
532 <https://doi.org/10.1016/B978-0-08-009235-5.50026-7>, 1960.

533

534 Morse, J. W. and Luther Iii, G. W.: Chemical influences on trace metal-sulfide interactions in
535 anoxic sediments, *Geochimica et Cosmochimica Acta*, 63, 3373-3378, [https://doi.org/10.1016/S0016-7037\(99\)00258-6](https://doi.org/10.1016/S0016-7037(99)00258-6), 1999.

537

538 Naik, V., Damare, S. R., Shah, S. S., Shenoy, D., and Mulla, A. B.: Effect of coastal hypoxia
539 on bacterial diversity as elucidated through 16S rRNA amplicon sequencing, *Frontiers in*
540 *Marine Science*, 11, 1301955, <https://doi.org/10.3389/fmars.2024.1301955>, 2024.

541

542 Naqvi, S., Jayakumar, D., Narvekar, P., Naik, H., Sarma, V., D'Souza, W., Joseph, S., and
543 George, M.: Increased marine production of N₂O due to intensifying anoxia on the Indian
544 continental shelf, *Nature*, 408, 346-349, <https://doi.org/10.1038/35042551>, 2000.

545

546 Naqvi, S. W. A., Naik, H., Jayakumar, D., Shailaja, M., and Narvekar, P.: Seasonal oxygen
547 deficiency over the western continental shelf of India, Past and present water column anoxia,
548 195-224, https://doi.org/10.1007/1-4020-4297-3_08, 2006.

549

550 Norði, K. A., Thamdrup, B., and Schubert, C. J.: Anaerobic oxidation of methane in an iron-
551 rich Danish freshwater lake sediment, *Limnology and Oceanography*, 58, 546-554,
552 <https://doi.org/10.4319/lo.2013.58.2.0546>, 2013.



553 Olson, L., Quinn, K. A., Siebecker, M. G., Luther Iii, G. W., Hastings, D., and Morford, J. L.:
554 Trace metal diagenesis in sulfidic sediments: Insights from Chesapeake Bay, *Chemical*
555 *Geology*, 452, 47-59, <https://doi.org/10.1016/j.chemgeo.2017.01.018>, 2017.

556

557 Oni, O., Miyatake, T., Kasten, S., Richter-Heitmann, T., Fischer, D., Wagenknecht, L.,
558 Kulkarni, A., Blumers, M., Shylin, S. I., and Ksenofontov, V.: Distinct microbial populations
559 are tightly linked to the profile of dissolved iron in the methanic sediments of the Helgoland
560 mud area, North Sea, *Frontiers in Microbiology*, 6, 365, [https://doi.org/10.3389/fmicb.2015.0](https://doi.org/10.3389/fmicb.2015.0365)
561 0365, 2015.

562

563 Orsi, W. D., Coolen, M. J. L., Wuchter, C., He, L., More, K. D., Irigoien, X., Chust, G.,
564 Johnson, C., Hemingway, J. D., and Lee, M.: Climate oscillations reflected within the
565 microbiome of Arabian Sea sediments, *Scientific Reports*, 7, 6040,
566 <https://doi.org/10.1038/s41598-017-05590-9>, 2017.

567 Parab, A. S., Ghose, M. P., and Manohar, C. S.: Variations in the bacterial community at
568 Chlorophyll Maximum (C-Max) depths along the west coast of India due to seasonal changes
569 in the primary productivity, *bioRxiv [preprint]*, 2023.2007.2005.547789,
570 <https://doi.org/10.1101/2023.07.05.547789>, 2023.

571 Parkes, R. J., Cragg, B. A., and Wellsbury, P.: Recent studies on bacterial populations and
572 processes in subseafloor sediments: a review, *Hydrology Journal*, 8, 11-28,
573 <https://doi.org/10.1007/PL00010971>, 2000.

574

575 Peketi, A., Mazumdar, A., Joao, H. M., Patil, D. J., Usapkar, A., and Dewangan, P.: Coupled
576 C-S-Fe geochemistry in a rapidly accumulating marine sedimentary system: diagenetic and
577 depositional implications, *Geochemistry, Geophysics, Geosystems*, 16, 2865-2883,
578 <https://doi.org/10.1002/2015GC005754>, 2015.

579

580 Peketi, A., Mazumdar, A., S.P.K, P., and Patil, D. J.: Influence of dual sulfate reduction
581 pathways on pore-fluid chemistry and occurrences of methane hydrate in sediment cores
582 (IODP-353) off Mahanadi basin, Bay of Bengal, *Geochemical Journal*, 54, 1-11,
583 <https://doi.org/10.2343/geochemj.2.0576>, 2020, 2020.

584



585 Pohlman, J. W., Ruppel, C., Hutchinson, D. R., Downer, R., and Coffin, R. B.: Assessing
586 sulfate reduction and methane cycling in a high salinity pore water system in the northern Gulf
587 of Mexico, *Marine and Petroleum Geology*, 25, 942-951, [https://doi.org/10.1016/j.
588 marpetgeo.2008.01.016](https://doi.org/10.1016/j.marpetgeo.2008.01.016), 2008.

589

590 Raghoebarsing, A. A., Pol, A., Van de Pas-Schoonen, K. T., Smolders, A. J. P., Ettwig, K. F.,
591 Rijpstra, W. I. C., Schouten, S., Damsté, J. S. S., Op den Camp, H. J. M., and Jetten, M. S. M.:
592 A microbial consortium couples anaerobic methane oxidation to denitrification, *Nature*, 440,
593 918-921, <https://doi.org/10.1038/nature04617>, 2006.

594

595 Raiswell, R., Vu, H. P., Brinza, L., and Benning, L. G.: The determination of labile Fe in
596 ferrihydrite by ascorbic acid extraction: methodology, dissolution kinetics and loss of solubility
597 with age and de-watering, *Chemical Geology*, 278, 70-79, [https://doi.org/10.1016/j.chemgeo.
598 2010.09.002](https://doi.org/10.1016/j.chemgeo.2010.09.002), 2010.

599

600 Ramírez-Pérez, A., De Blas, E., and García-Gil, S.: Redox processes in pore water of anoxic
601 sediments with shallow gas, *Science of the Total Environment*, 538, 317-326,
602 <https://doi.org/10.1016/j.scitotenv.2015.07.111>, 2015.

603

604 Rickard, D. and Luther III, G. W.: Chemistry of iron sulfides, *Chemical reviews*, 107, 514-562,
605 <https://doi.org/10.1021/cr0503658>, 2007.

606

607 Riedinger, N., Formolo, M. J., Lyons, T. W., Henkel, S., Beck, A., and Kasten, S.: An inorganic
608 geochemical argument for coupled anaerobic oxidation of methane and iron reduction in
609 marine sediments, *Geobiology*, <https://doi.org/10.1111/gbi.12077>, 2014.

610

611 Scheller, S., Yu, H., Chadwick, G. L., McGlynn, S. E., and Orphan, V. J.: Artificial electron
612 acceptors decouple archaeal methane oxidation from sulfate reduction, *Science*, 351, 703-707,
613 <https://doi.org/10.1126/science.aad7154>, 2016.

614

615 Schott, F. A. and McCreary Jr, J. P.: The monsoon circulation of the Indian Ocean, *Progress in
616 Oceanography*, 51, 1-123, [https://doi.org/10.1016/S0079-6611\(01\)00083-0](https://doi.org/10.1016/S0079-6611(01)00083-0), 2001.

617



- 618 Segarra, K. E. A., Comerford, C., Slaughter, J., and Joye, S. B.: Impact of electron acceptor
619 availability on the anaerobic oxidation of methane in coastal freshwater and brackish wetland
620 sediments, *Geochimica et Cosmochimica Acta*, 115, 15-30, [https://doi.org/10.1016/j.gca.2013.](https://doi.org/10.1016/j.gca.2013.03.029)
621 03.029, 2013.
- 622
- 623 Sivan, O., Adler, M., Pearson, A., Gelman, F., Bar-Or, I., John, S. G., and Eckert, W.:
624 Geochemical evidence for iron-mediated anaerobic oxidation of methane, *Limnology and*
625 *Oceanography*, 56, 1536-1544, <https://doi.org/10.4319/lo.2011.56.4.1536>, 2011.
- 626
- 627 Slomp, C. P., Mort, H. P., Jilbert, T., Reed, D. C., Gustafsson, B. G., and Wolthers, M.: Coupled
628 dynamics of iron and phosphorus in sediments of an oligotrophic coastal basin and the impact
629 of anaerobic oxidation of methane, *PloS one*, 8, e62386, [https://doi.org/10.1371/journal.pone.](https://doi.org/10.1371/journal.pone.0062386)
630 0062386, 2013.
- 631
- 632 Torres, M. E., Mix, A. C., and Rugh, W. D.: Precise $\delta^{13}\text{C}$ analysis of dissolved inorganic carbon
633 in natural waters using automated headspace sampling and continuous-flow mass spectrometry.
634 *Limnology and Oceanography: Methods*, 3, 349-360, <https://doi.org/10.4319/lom.2005.3.349>,
635 2005.
- 636
- 637 Treude, T., Krause, S., Maltby, J., Dale, A. W., Coffin, R., and Hamdan, L. J.: Sulfate reduction
638 and methane oxidation activity below the sulfate-methane transition zone in Alaskan Beaufort
639 Sea continental margin sediments: Implications for deep sulfur cycling, *Geochimica et*
640 *Cosmochimica Acta*, 144, 217-237, <https://doi.org/10.1016/j.gca.2014.08.018>, 2014.
- 641
- 642 Vigderovich, H., Liang, L., Herut, B., Wang, F., Wurgaft, E., Rubin-Blum, M., and Sivan, O.:
643 Evidence for microbial iron reduction in the methanic sediments of the oligotrophic
644 southeastern Mediterranean continental shelf, *Biogeosciences*, 16, 3165-3181,
645 <https://doi.org/10.5194/bg-16-3165-2019>, 2019.
- 646
- 647 Volvoikar, S., Mazumdar, A., Peketi, A., Dewangan, P., Sawant, B., Manaskanya, A.,
648 Goswami, H., Das, D., and Pujari, S.: Contrasting sulfidization in the turbidite and hemipelagic
649 sediments of Bengal Fan, *Marine and Petroleum Geology*, 118, 104408,
650 <https://doi.org/10.1016/j.marpetgeo.2020.104408>, 2020.



651

652 Wegener, G., Krukenberg, V., Riedel, D., Tegetmeyer, H. E., and Boetius, A.: Intercellular
653 wiring enables electron transfer between methanotrophic archaea and bacteria, *Nature*, 526,
654 587-590, <https://doi.org/10.1038/nature15733>, 2015.

655

656 Wegener, G., Gropp, J., Taubner, H., Halevy, I., and Elvert, M.: Sulfate-dependent reversibility
657 of intracellular reactions explains the opposing isotope effects in the anaerobic oxidation of
658 methane, *Science Advances*, 7, eabe4939, <https://doi.org/10.1126/sciadv.abe4939>, 2021.

659

660 Whiticar, M. J.: Isotope tracking of microbial methane formation and oxidation, *Internationale*
661 *Vereinigung für Theoretische und Angewandte Limnologie: Mitteilungen*, 25, 39-54,
662 <https://doi.org/10.1080/05384680.1996.11904065>, 1996.

663

664 Whiticar, M. J.: Carbon and hydrogen isotope systematics of bacterial formation and oxidation
665 of methane, *Chemical Geology*, 161, 291-314, [https://doi.org/10.1016/S0009-2541\(99\)00092-](https://doi.org/10.1016/S0009-2541(99)00092-3)
666 3, 1999.

667

668 Xiao, X., Luo, M., Zhang, C., Zhang, T., Yin, X., Wu, X., Zhao, J., Tao, J., Chen, Z., and Liang,
669 Q.: Metal-driven anaerobic oxidation of methane as an important methane sink in methanic
670 cold seep sediments, *Microbiology Spectrum*, 11, e05337-05322,
671 <https://doi.org/10.1128/spectrum.05337-22>, 2023.

672

673 Yoshinaga, M. Y., Holler, T., Goldhammer, T., Wegener, G., Pohlman, J. W., Brunner, B.,
674 Kuypers, M. M. M., Hinrichs, K.-U., and Elvert, M.: Carbon isotope equilibration during
675 sulphate-limited anaerobic oxidation of methane, *Nature Geoscience*, 7, 190-194,
676 <https://doi.org/10.1038/ngeo2069>, 2014.

677

678 **Supplementary Data.** For figures (Figures S1 and S2), tables (Tables S1, S2 and S3), and
679 supporting text, please see supplementary data file.

680

681